Capacitance of graphene nanoribbons

A. A. Shylau,[1] J. W. Kłos,[1,2] and I. V. Zozoulenko[1]
[1]*Solid State Electronics, ITN, Linköping University, 601 74 Norrköping, Sweden*
[2]*Surface Physics Division, Faculty of Physics, Adam Mickiewicz University, Umultowska 85, 61-614 Poznan, Poland*
(Received 6 July 2009; revised manuscript received 3 September 2009; published 4 November 2009)

We present an analytical theory for the gate electrostatics and the classical and quantum capacitance of the graphene nanoribbons (GNRs) and compare it with the exact self-consistent numerical calculations based on the tight-binding *p*-orbital Hamiltonian within the Hartree approximation. We demonstrate that the analytical theory is in a good qualitative (and in some aspects quantitative) agreement with the exact calculations. There are however some important discrepancies. In order to understand the origin of these discrepancies we investigate the self-consistent electronic structure and charge density distribution in the nanoribbons and relate the above discrepancy to the inability of the simple electrostatic model to capture the classical gate electrostatics of the GNRs. In turn, the failure of the classical electrostatics is traced to the quantum mechanical effects leading to the significant modification of the self-consistent charge distribution in comparison to the noninteracting electron description. The role of electron-electron interaction in the electronic structure and the capacitance of the GNRs is discussed. Our exact numerical calculations show that the density distribution and the potential profile in the GNRs are qualitatively different from those in conventional split-gate quantum wires; at the same time, the electron distribution and the potential profile in the GNRs show qualitatively similar features to those in the cleaved-edge overgrown quantum wires. Finally, we discuss an experimental extraction of the quantum capacitance from experimental data.

DOI: 10.1103/PhysRevB.80.205402 PACS number(s): 73.21.−b, 73.22.−f, 73.20.−r, 81.05.Uw

I. INTRODUCTION

Graphene, a two-dimensional (2D) honeycomb structure of carbon atoms, has attracted a lot of interest since its isolation in 2004.[1] It demonstrates unique properties which originate from the Dirac-type spectrum of low-energy quasiparticles. Nowadays, graphene is considered to be a viable alternative to Si for the channel of field-effect transistors (FETs).[2] One of the main characteristics of such devices is a capacitance formed between the channel and the gate. The capacitance is important for understanding fundamental electronic properties of the material such as the density of states (DOS) as well as device performance including the *I*-*V* characteristics and the device operation frequency.

In a classical regime, the capacitance describes the capability of an object to store electrical charges and is completely determined by the object's geometry and a dielectric constant of the medium. If the object's size shrinks to a nanometer scale, quantum effects have to be taken in account. One of manifestations of these effects is a finite DOS which originates from the Pauli exclusion principle. Low-dimensional systems, having a small DOS, are not able to accumulate enough charge to completely screen the external field. In order to describe the effect of the electric field penetration through a two-dimensional electronic gas (2DEG) Luryi introduced a concept of a quantum capacitance.[3]

Recently, the quantum capacitance of a bulk graphene layer deposited on a gated SiO_2 insulated surface has been investigated by means of scanning probe microscopy.[4] To the best of our knowledge, no studies of the gate capacitance of the graphene nanoribbons (GNRs) have been reported yet. However, such studies are already technologically feasible. Indeed, during last years the great progress has been achieved in fabrication and patterning of the GNRs (Refs. 5–8) as well as in controlling the morphology, geometry, and stability of the graphene edges.[9,10] On the other hand, the quantum and classical capacitance of related structures—carbon nanotubes has been measured and analyzed by a number of groups during the last years.[11–14] The later studies have revealed a number of interesting properties of the system at hand including the structure of the DOS and signatures of the electron interaction and correlation.

In order to provide physical insight into the gate electrostatics and capacitance of the GNRs, it is important to develop intuitive analytical models capturing the essential physics of the device at hand. Such models are also imperative in experimental measurements because the quantum capacitance is not directly accessible in the experiments and can only be indirectly extracted from the measured total capacitance. In the present paper we develop a basic analytical theory for the gate electrostatics and the classical and quantum capacitance of the GNRs. We complement this analytical theory by exact self-consistent numerical calculations based on the tight-binding *p*-orbital Hamiltonian within the Hartree approximation. We demonstrate that the analytical theory is in a good qualitative (and in some aspects quantitative) agreement with the exact calculations. There are however some important discrepancies. In order to understand the origin of these discrepancies we investigate the self-consistent electronic structure and charge density distribution in the nanoribbons and relate the above discrepancy to the inability of the simple electrostatic model to capture the classical gate electrostatics of the GNRs. In turn, the failure of the classical electrostatics is traced to the quantum mechanical effects leading to the significant modification of the self-consistent charge distribution in comparison to the noninteracting electron description.

It should be noted that particular aspects of the self-consistent gate electrostatics and the electron structure of the

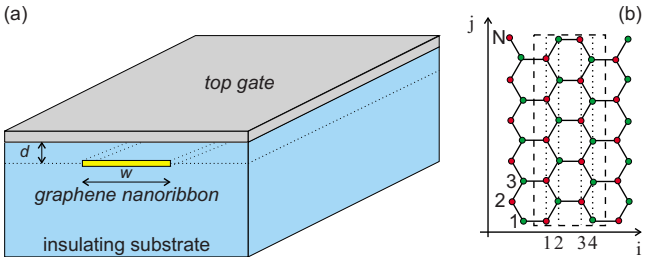

FIG. 1. (Color online) (a) A schematic diagram illustrating a top-gate geometry where an infinitely long graphene nanoribbon of the width w is embedded in a gate insulator with the relative dielectric constant ϵ_r; d is the distance between the ribbon and the top gate. It is assumed that the graphene nanoribbon is connected to the source and drain reservoirs supplying electrons to the ribbon. (b) An armchair graphene ribbon of the width N. Unit cell consisting of $2N$ sites is marked with dashed rectangle. All the results presented in this paper correspond to $N=98$($w=12$ nm).

GNRs (Ref. 15) and the numerical[16] and analytical[17] studies of quantum capacitance of the GNRs have been reported in the literature. In particular, the quantum capacitance of the GNRs as a function of the Fermi energy, $C_Q=C_Q(E_F)$, has been studied in Ref. 17. Experimentally, however, the dependence of C_Q on the Fermi energy is not accessible, and we stress that the focus of our analytical and numerical analysis is the gate capacitance, $C=C(V_g)$—the characteristic that is measured experimentally (V_g being the gate voltage).

The paper is organized as follows. In Sec. II we formulate the basics of our model of the gated GNRs. The analytical treatment of the gate electrostatics and the quantum and classical gate capacitance of GNRs is given in Sec. III. The results of the self-consistent numerical calculations and a comparison between the analytical and numerical calculations are presented and discussed in Sec. IV. Section V summarizes the main conclusions.

II. MODEL

In experiments graphene samples are separated from the gate by a relatively thick insulating substrate (of a typical width of at least 300 nm) in order to enable visual identification of the graphene sheet. This simplest experimental setup (with a single back gate) is not particularly suitable for measurements of the quantum capacitance because in this case (as we will demonstrate below) the total capacitance is completely dominated by the classical contribution and can hardly be extracted from the measured total capacitance. In order to distinguish the quantum contribution the gate should be placed much closer to the ribbon such that the classical capacitance C_C becomes comparable to the quantum one. In our study we therefore consider an embedded top-gate geometry shown in Fig. 1 where a graphene ribbon of the width w is placed on a thick dielectric layer and covered by the second much thinner layer of the width d separating it from the top gate with the applied gate voltage V_g. This top-gate geometry was used by Ilani *et al.*[11] and Natori *et al.*[18] for measurements of the quantum capacitance of carbon nanotubes. We also assume that the GNR is connected to the source and drain electrods playing a role of ideal reservoirs supplying electrons to the ribbon. The experimental setup might also include the back gate which can, independently of the top gate, adjust a position of the Dirac point in the graphene nanoribbon, and hence change its electron density. However we assume that the back gate is situated much further apart from the ribbon in comparison to the top gate, and therefore for the sake of simplicity we in our model disregard a possible capacitative coupling between the ribbon and the back gate.

In this paper we considered two representative structures, (I) HfO_2 insulating layer with $d=30$ nm and $\varepsilon_r=47$,[15,19,20] and (II) SiO_2 insulating layer with $d=300$ nm and $\varepsilon_r=3.9$. For the first structure C_C is comparable to C_Q, whereas for the second one $C_C \ll C_Q$. We limit our calculations to the case of the armchair GNRs, whereas we expect that the main results and conclusions presented in this paper can be extended to the case of the zigzag GNRs. (Note that we do not focus on any specific peculiarities of the DOS near the Dirac point like surface states in the case of zigzag ribbons). The spin effects and the effect of disorder are outside the scope of our paper and are deferred to future studies. All results correspond to the metallic armchair GNRs with the width $w=12$ nm ($N=98$). We also made calculations for a semiconductor armchair GNR as well as for wider ribbons ($w=50$ nm) and all the results show the same features.

The system presented on Fig. 1 is described by the standard p-orbital tight-binding Hamiltonian[21,22]

$$H = \sum_{\mathbf{r}} V_H(\mathbf{r}) a_{\mathbf{r}}^{+} a_{\mathbf{r}} - \sum_{\mathbf{r},\Delta} t_{\mathbf{r},\mathbf{r}+\Delta} a_{\mathbf{r}}^{+} a_{\mathbf{r}+\Delta}, \tag{1}$$

where $t_{\mathbf{r},\mathbf{r}+\Delta}=2.5$ eV is a nearest-neighbor hopping integral; $V_H(\mathbf{r})$ is a Hartree potential at the site $\mathbf{r}$ which results from the Coulomb interaction between extra charges in the system (including the mirror charges),[15,23–25]

$$V_H(\mathbf{r}) = \frac{e^2}{4\pi\varepsilon_0\varepsilon_r} \sum_{\mathbf{r}' \neq \mathbf{r}} q(\mathbf{r}') \left(\frac{1}{|\mathbf{r}-\mathbf{r}'|} - \frac{1}{\sqrt{|\mathbf{r}-\mathbf{r}'|^2+4d^2}} \right), \tag{2}$$

where $q(\mathbf{r})$ is the local electron occupation, and the second term in the parenthesis corresponds to the mirror charges. The summation in Eq. (2) can be split into two parts corresponding to the A and B sublattices of graphene [see Fig. 1(b)]. Changing summation to integration in the i direction we obtain,

$$V_H(\mathbf{r}_{ij}) = -\frac{e^2}{4\pi\varepsilon_0\varepsilon_r} \sum_{j'=1(j'\neq j)}^{N} \frac{q_A(j')+q_B(j')}{2} \times \ln \frac{(\mathbf{r}_{ij}-\mathbf{r}_{ij'})^2}{(\mathbf{r}_{ij}-\mathbf{r}_{ij'})^2+4d^2}, \tag{3}$$

where $q_{A(B)}(j')$ is the charge on the carbon atom which is located on the j' line and corresponds to the $A(B)$ sublattice.

We solve Eq. (1) numerically to find the Green's function using the technique described by Xu *et al.*[26] This technique greatly facilitates computation speed since it does not require self-consistent calculation of the surface Green's function.

The Green's function in the real-space representation, $G(\mathbf{r},\mathbf{r})$, provides an information about the local density of states (LDOS) at site $\mathbf{r}$,

$$\rho(\mathbf{r},E) = -\frac{2}{\pi S}\Im\{[G(\mathbf{r},\mathbf{r})]\}, \tag{4}$$

where factor 2 indicates a spin degeneracy and $S=\frac{a^2\sqrt{3}}{4}$ is the area corresponding to one carbon atom in the graphene lattice, with $a=0.246$ nm being the lattice constant. The LDOS can be used to calculate the local electron density at the site $\mathbf{r}$,

$$n(\mathbf{r},E_F) = \int_{eV_C}^{E_F} dE\rho(\mathbf{r},E)f_{FD}(E-E_F), \tag{5}$$

where $E_F=eV_g$ is Fermi energy and f_{FD} is the Fermi-Dirac distribution function. (All the calculations reported in this paper correspond to the temperature $T=0$ K.) The position of the charge neutrality point eV_C at a given gate voltage V_g is determined numerically from the calculated dispersion relation. For example, for the armchair GNRs, the position of the charge neutrality point eV_C corresponds to the energy which gives the minimum number of propagating states with the smallest absolute value of the wave vector. Note, that in order to achieve a fast convergence, the itegration in Eq. (5) is performed in a complex plane, since on the real E axis $\rho(\mathbf{r},E)$ is a rapidly varying function of the energy (see Refs. 23 and 24 for details).

Since the Hartree potential V_H (3) depends on the electron density $n(\mathbf{r})$ which is a solution of the Schrödinger equation with the Hamiltonian (1), these equations need to be solved iteratively. The iteration process is executed until the convergence criterion is met, $|\frac{V^m_{\text{out}}-V^m_{\text{in}}}{V^m_{\text{out}}+V^m_{\text{in}}}|<10^{-5}$, where V^m_{in} and V^m_{out} are the input and output average values of the Hartree potential on the m-th iteration. In order to accelerate convergence we used the Broyden's second method,[27] which allows us to reduce the number of iterations to $\sim 8-10$ in comparison to $\sim 40-50$ iterations needed with the "simple mixing" method.

Having calculated the electron density and the position of the Dirac point numerically, we are in position to find the total, quantum and classical capacitances as a function of the gate voltage, see Sec. IV for details. The analytical approach to the quantum and classical capacitance of the GNRs is described in the next section.

III. CLASSICAL AND QUANTUM CAPACITANCE OF GRAPHENE NANORIBBONS: AN ANALYTICAL MODEL

The electronic structure of planar gated graphene sheets was studied by Fernández-Rossier *et al.*[15] In this section we follow the approach outlined by Fernández-Rossier *et al.*[15] and provide an analytical description of the one-dimensional charge density and quantum and classical capacitance of the graphene nanoribbons.

Application of the gate voltage V_g to a metallic gate induces extra carriers with the density n to the nanoribbon as well as extra carriers of the opposite polarity to the gate itself. (Note that the gate and the ribbon represent together a charge neutral system). The application of the gate voltage shifts the chemical potential μ of the ribbon from the charge neutrality point μ_0,[15]

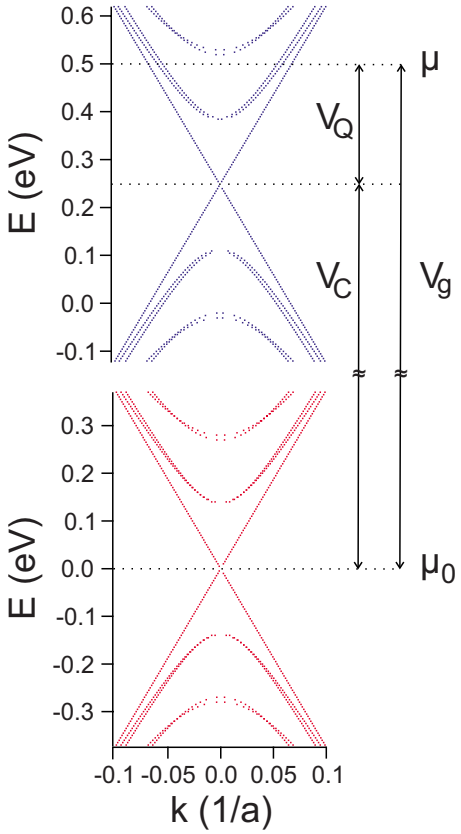

FIG. 2. (Color online) A diagram illustrating the change in the band structure of the graphene nanoribbon. Application of the gate voltage V_g results in a shift of the chemical potential from the charge neutrality point μ_0 to μ. This shift can be presented as a sum of two contributions, eV_C, the rigid shift of bands, and eV_Q, the shift of the chemical potential with respect to the charge neutrality point leading to an electron doping of the system. The displayed diagram corresponds to the HfO_2 structure with $d=30$ nm and $V_g=0.5$ V.

$$eV_g = \mu - \mu_0, \tag{6}$$

It is convenient to represent this shift as a sum of two terms

$$\mu - \mu_0 = eV_C + eV_Q, \tag{7}$$

where eV_C describes the position of the charge neutrality point at the applied voltage V_g, and eV_Q describes the change in the chemical potential due to the filling of the quantum mechanical energy bands, see Fig. 2 for illustration. For a classical conductor the density of states is infinite and thus $V_Q=0$. This provides a natural interpretation of V_C as a classical electrostatic potential, whereas the potential V_Q has a quantum mechanical origin reflecting the structure of the quantum-mechanical density of states. Using a relation

$$V_g = V_Q + V_C, \tag{8}$$

which follows from Eqs. (6) and (7) and using a definition of a capacitance $C=\frac{e\partial n}{\partial V}$, we obtain[15]

$$C_{\text{tot}}^{-1} = C_C^{-1} + C_Q^{-1}, \tag{9}$$

where the total capacitance $C_{\text{tot}} = \frac{e\partial n}{\partial V_g}$, and the classical and the quantum-mechanical capacitances are respectively $C_C = \frac{e\partial n}{\partial V_C}$ and $C_Q = \frac{e\partial n}{\partial V_Q}$.

In order to find the total capacitance for a given gate voltage we have to calculate the electron density n. The later at the zero temperature is given by

$$n = \int_{-\infty}^{\mu} \rho(E)dE - \int_{-\infty}^{\mu_0} \rho_0(E)dE, \tag{10}$$

where $\rho_0(E)$ is the density of states for a charge neutral ribbon ($\mu=\mu_0$), $\rho(E)$ is the DOS at $\mu=\mu_0+eV_g$. (In the following we will refer to the case $V_g=0$ as to an uncharged ribbon, and to the case of $V_g \neq 0$ as a charged ribbon.) In the analytical model we assume that application of the gate voltage results in a rigid shift of the bands on the value eV_C and does not change their relative position in respect to the charge neutrality point

$$\rho(E) = \rho_0(E - eV_C). \tag{11}$$

In the next section we will demonstrate that this approximation holds extremely well despite of some modifications of the band structure for higher gate voltages. Substituting Eq. (11) into Eq. (10) and performing the change in variables, the density of the extra carriers reads[15]

$$n = \int_{eV_C}^{\mu} \rho(E)dE = \int_{\mu_0}^{\mu_0+eV_Q} \rho_0(E)dE, \tag{12}$$

which means that the extra carriers occupy the bands in the energy interval between the charge neutrality point and the chemical potential.

The DOS of graphene armchair nanoribbons can be written in the form (see Appendix A)

$$\rho_0(E) = \frac{4}{\pi\sqrt{3}ta} \sum_n \frac{|E|}{\sqrt{E^2 - E_n^2}} \theta(|E| - |E_n|), \tag{13}$$

where $n=0, \pm 1, \pm 2, \ldots$, $a=0.246$ nm is the graphene lattice constant (note that $\frac{\sqrt{3}}{2}ta = v_F\hbar$ with v_F being the Fermi velocity), and E_n are the subband threshold energies whose analytical expressions are provided by Onipko[28] (see Appendix A for the explicit expressions for E_n). Substituting this expression of the DOS into Eq. (12), we obtain for the one-dimensional (1D) electron density of the nanoribbon,

$$n(V_Q) = \frac{4}{\pi\sqrt{3}ta} \sum_n \sqrt{(eV_Q)^2 - E_n^2}\, \theta(|eV_Q| - |E_n|), \tag{14}$$

where $n=0, \pm 1, \pm 2, \ldots$. Here and hereafter without loss of generality we set $\mu_0=0$. Using the definition of the quantum capacitance we get,[17]

$$C_Q = \frac{e\,\partial n}{\partial V_Q} = e^2 \rho_0(eV_Q). \tag{15}$$

In order to calculate C_Q from the above equation we have to know the position of the chemical potential with respect to the charge neutrality point of the charged ribbon, eV_Q. This can be done from Eq. (8), where the classical electrostatic potential can be easily calculated using the standard method of images (see Appendix B for details),

$$V_C = \frac{\sigma}{\pi\varepsilon_0\varepsilon_r}\left[2d \arctan\frac{w}{4d} + \frac{w}{4}\ln\left\{1 + \left(\frac{4d}{w}\right)^2\right\}\right], \tag{16}$$

(the definitions of w and d are given in Fig. 1). In the derivation of this expression we assumed that the surface charge density of the graphene nanoribbon $\sigma=n/w$ is constant (as expected for a classical capacitor). We will discuss the validity of this assumption in the next section. The classical capacitance (per unit length) of the graphene nanoribbon follows from Eq. (16),

$$C_C = \frac{e\,\partial n}{\partial V_C} = \pi\varepsilon_0\varepsilon_r w\left[2d \arctan\frac{w}{4d} + \frac{w}{4}\ln\left\{1 + \left(\frac{4d}{w}\right)^2\right\}\right]^{-1}. \tag{17}$$

Note that in the limit of a narrow ribbon, $w \ll d$, the above expression simplifies to $C_C = 2\pi\varepsilon_0\varepsilon_r / \ln\frac{4d}{w}$.

To summarize, Eqs. (8), (9), and (14)–(17) provide the analytical expressions for the 1D electron density and the total, quantum, and classical capacitances of the graphene nanoribbons. In order to express the density and the capacitances as a function of the gate voltage V_g (rather than V_Q which is not accessible experimentally) we first choose some value of V_Q and calculate n and C_Q from Eqs. (14) and (15). We then use the calculated values in Eqs. (16) and (17) to find corresponding V_C and C_C. Finally, relating V_Q to V_g via Eq. (8), we express the density and the capacitances as a function of the gate voltage V_g.

IV. RESULTS AND DISCUSSION

Figure 3 shows the analytical and numerical densities and capacitances for two representative nanoribbon structures introduced in Sec. II. The left column corresponds to the 30 nm HfO_2 dielectric structure with $\varepsilon_r=47$, and the right column corresponds to a conventional 300 nm SiO_2 structure with $\varepsilon_r=3.9$. The analytical results are based on the expressions given by Eqs. (8), (9), and (14)–(17) and show the electron density n, the total, quantum, and classical capacitances C_{tot}, C_Q, C_C [Figs. 3(a)–3(d), respectively].

The numerical results are based on the self-consistent solution of Eqs. (1)–(5) as described in Sec. II. We first calculate the electron density as a function of the gate voltage and then differentiate it numerically in order to compute the total capacitance, $C_{\text{tot}} = \frac{e\partial n}{\partial V_g}$, see Figs. 3(a) and 3(b) respectively. Figure 3(c) shows the quantum capacitance C_Q which is calculated from the DOS on the basis of Eq. (15) (note that $\rho_0(E) = \frac{1}{2N}\Sigma_{\mathbf{r}}\rho(\mathbf{r},E)$, where $\rho(\mathbf{r},E)$ is the LDOS given by Eq. (4), and summation is performed over one unit cell containing $2N$ sites). Having calculated C_{tot} and C_Q we compute the classical capacitance from Eq. (9) as $C_C^{-1} = C_{\text{tot}}^{-1} - C_Q^{-1}$, see Fig. 3(d).

The total capacitance C_{tot} for both structures shows characteristic features that can be traced to the corresponding features in the quantum capacitance C_Q, [cf. Figs. 3(b) and

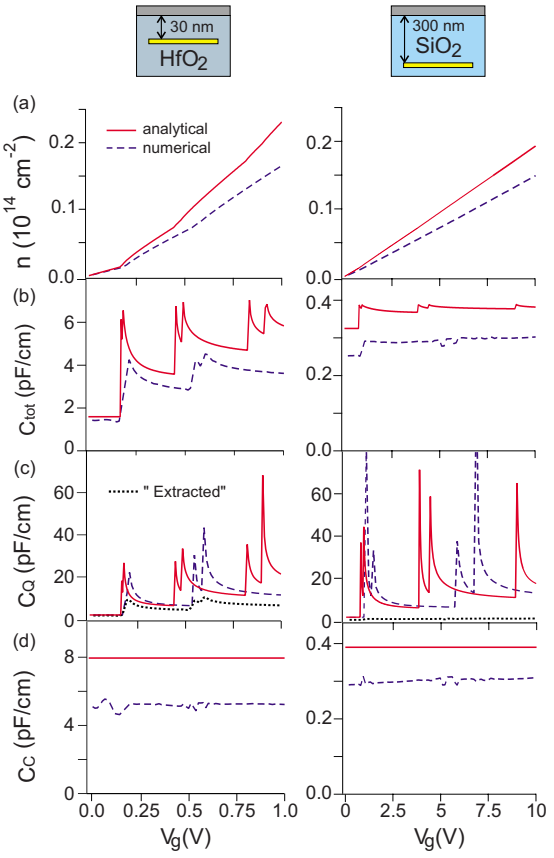

FIG. 3. (Color online) The analytical and numerical dependencies on the applied gate voltage of (a) the electron density n, (b) the total capacitance C_{tot}, (c) the quantum capacitance C_Q, and (d) the classical capacitance C_C. (c) also shows the "extracted" quantum capacitance (see text for details). Left and right panels corresponds, respectively, to HfO_2 and SiO_2 structures.

3(c)]. Because the quantum capacitance is proportional to the DOS [see Eq. (15)] the peaks in C_Q signal consecutive population of electron subbands as the gate voltage increases. Note that these features in C_{tot} are much less pronounced for the case of a conventional SiO_2 structure because its classical capacitance is much smaller than the quantum one ($C_Q/C_C \sim 40$), whereas for the HfO_2 structure this ratio is only ~ 2 [note that the quantum and classical capacitances are added in series, Eq. (9)].

The comparison of the analytical and numerical calculations demonstrates that the analytical theory qualitatively reproduces the exact results very well. There is however some quantitative discrepancy in the values of both quantum and classical capacitances. In particular, the analytical classical capacitance differs by 20%–35% from its exact numerical value, see Fig. 3(d). For the case of the SiO_2 structure the numerical C_C shows a slow increase as V_g increases. This is in apparent contrast with the behavior of its analytical counterpart which is independent of the applied voltage. As far as the quantum capacitance is concerned, a visual inspection of Fig. 3(c) indicates that the analytical and numerical C_Q would coincide if one stretches the scale of V_g for the analytical capacitance (alternatively contracts the scale of V_g for the numerical capacitance).

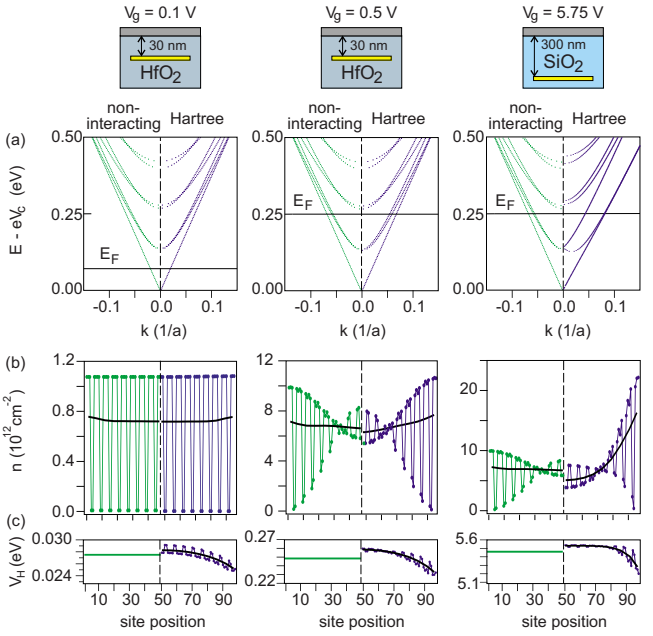

FIG. 4. (Color online) A comparison between the noninteracting case (left parts of the panels) and the self-consistent Hartree model (right parts) for the HfO_2 structure with $V_g=0.1$ V (first column), HfO_2 structure with $V_g=0.5$ V (second column), and SiO_2 structure with $V_g=5.75$ V (third column). (a) The band structure of the nanoribbons; thin solid lines indicate the positions of the Fermi energy. (b) The electron density distribution across the nanoribbon. (c) The potential profiles in the Hartree approximation (right parts); the numerically calculated value of V_C (left parts). In (b) and (c) the black lines indicate the values of the electron density and the Hartree potential averaged over several neighboring sites.

In order to understand the differences between the analytical and the exact results let us critically inspect the assumptions that have been made in the derivation of the analytical expressions in the previous section. Let us start with the classical capacitance C_C given by Eq. (17). In its derivation (see Appendix B) we assumed that the induced charge density is homogeneous and the potential of the ribbon is constant as expected for a classical conductor. Figures 4(b) and 4(c) show, respectively, the electron density distributions and the Hartree potential for the various nanoribbon structures for different values of V_Q and thus for different densities n [Note that the amount of the induced charge density n is completely determined by the value of V_Q defining the position of the Fermi energy with respect to the charge neutrality point, Eqs. (12) and (14). For a reference purpose, the values of V_Q are indicated at the corresponding dispersion relations shown in Fig. 4(a)]. In order to outline the role of the electron-electron interaction we show both the self-consistent Hartree and the noninteracting one-electron calculations (respectively, right and left parts of the panels in Fig. 4).

The electron density distribution in the GNRs shows the pronounced oscillation between neighboring sites. We therefore also show the electron density averaged over several neighboring sites, Fig. 4(b). For a small gate voltage (HfO_2 structure, $V_g=0.1$ V) when only the first subband is filled the averaged electron density distribution is almost uniform and

there is practically no difference between the self-consistent and the one-electron approaches. By increasing the gate voltage to $V_g=0.5$ V more carriers are induced and the electron density increases near the edges of the structure due to the electrostatic repulsion. It is important to stress that it is not only the concentration of the induced charge but primarily the applied gate voltage that determine the charge density distribution. Figure 4(b) shows the electron-density distribution and the potential profile for the SiO_2 structure for the gate voltage $V_g=5.75$ V. This gate voltage is chosen such that the value of $V_Q=0.25$ eV is the same as for the HfO_2 structure with $V_g=0.5$ V [see Fig. 4(a)], i.e., the induced charge concentrations are similar. However, the density distribution profile for the SiO_2 structure is strikingly different showing a strong redistribution of the charges toward the edges when the applied voltage is increased. The larger the applied voltage, the stronger the redistribution of the electron density. This explains the observation that the numerical C_C gradually changes when the gate voltage is increased [see Fig. 3(d), right panel]. We therefore conclude that the assumptions appropriate for a classical capacitor (the charge density is homogeneous and the potential of the ribbon V_C is constant) are violated for the graphene nanoribbons which leads to the difference between the analytical theory and the exact numerical calculations.

Note that the macroscopic charge accumulation along the boundaries of the graphene strip was discussed by Silvestrov and Efetov.[29] Their semiclassical approach and the exact numerical calculations presented here demonstrate that the density distribution and the potential profile in the GNRs are qualitatively different from those in conventional split-gate quantum wires with a smooth electrostatic confinement where the potential is rather flat and the electron density is constant throughout the wire.[23] At the same time, the electron distribution and the potential profile in the GNR are very similar to those in the cleaved-edge overgrown quantum wires (CEOQW). Indeed, the potential profile in the CEOQWs also exhibits triangular-shaped quantum wells in the vicinity of the wire boundaries and the electron density is also strongly enhanced close to the edges.[24] This similarity simply reflects the fact that both the CEOQWs and the GNRs correspond to the case of the hard-wall confinement at the edges of both structures. Let us now discuss the quantum capacitance C_Q and the difference between the corresponding analytical and numerical results. The crucial assumption used in the analytical model is that an application of the gate voltage V_g simply shifts the bands on the amount V_C such that the DOS of the GNR remains unchanged relatively to the charge neutrality point for any V_g, Eq. (11). Because the amount of the induced charges is completely determined by the value of V_Q (Eq. (14)), this assumption implies that the dependence $n=n(V_Q)$ obtained by both analytical and numerical calculations should coincide. In order to verify this assumption we compare the evolution of the band diagram for structures with different classical capacitances for different gate voltages. Figure 5(a) shows the dispersion relation for HfO_2 and SiO_2 structures where the gate voltages V_g are chosen such that V_Q is the same in both cases ($V_Q=0.25$ V for $V_g^{HfO_2}=0.5$ V and $V_g^{SiO_2}=5.75$ V). (For comparison we also display the dispersion relations for noninteracting electrons). Even though the equal values of V_Q imply the same induced charge density, the changes of the dispersion relations are quite different. In the considered V_g interval the dispersion relation of the HfO_2 structure remains practically unchanged, and therefore the analytical and the numerical dependencies for $n=n(V_Q)$ as well as for $C_Q=C_Q(V_Q)$ are almost undistinguished [see Figs. 5(b) and 5(c), left panels]. Modification of the band structure is much stronger for the case of the SiO_2 structure with smaller C_C. This is also reflected in the analytical and numerical dependencies $n=n(V_Q)$ exhibiting a difference up to 15% in the considered gate voltage interval. However, despite of this difference for $n=n(V_Q)$ the corresponding difference between the analytical and numerical results for $C_Q=C_Q(V_Q)$ is practically negli-

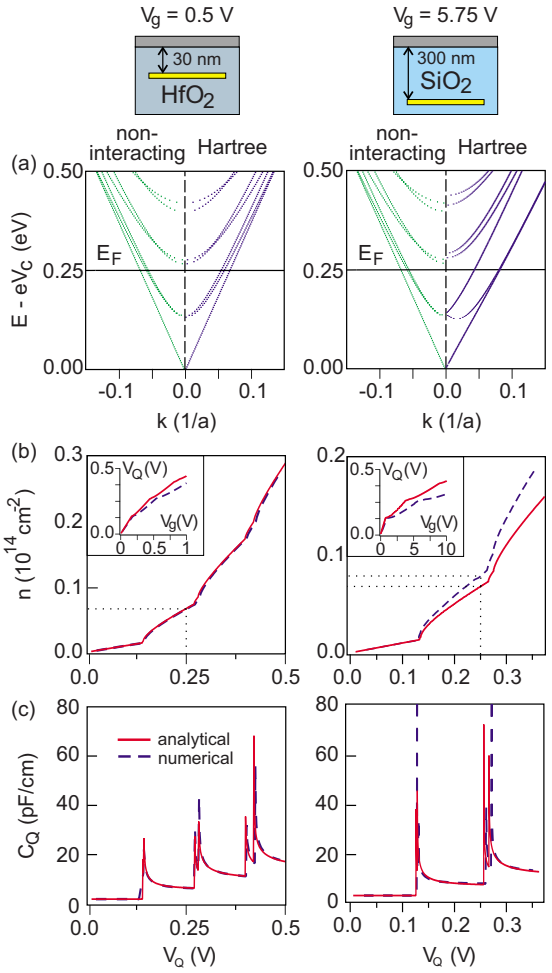

FIG. 5. (Color online) (a) The dispersion relations for the noninteracting and the Hartree electrons (left and right parts of the diagrams, respectively). For the Hartree case the dispersion relation is calculated for $V_Q=0.25$ V; the corresponding values of V_g are indicated above the figure. (b) Analytical (solid lines) and numerical (dashed lines) electron concentration n and (c) quantum capacitance C_Q as a function of the Fermi energy level with respect to the Dirac point (V_Q). The dotted lines serve as a guide to compare the analytical and numerical electron densities calculated for $V_Q=0.25$ V. The insets in (b) show the dependence of V_Q on the applied gate voltage V_g. Left and right panels corresponds respectively to HfO_2 and SiO_2 structures.

gible even for the SiO_2 structure, see Figs. 5(b) and 5(c), right column.

The reason for the modification of the band structure can be understood from the analysis of the potential distribution shown in Fig. 4(c). In order to shift V_Q on the same value one should apply a higher gate voltage to the structure with a smaller classical capacitance. Different gate voltages applied to different structures produce the same shift of V_Q but give rise to different distributions of the electrostatic potential across the nanoribbon. The difference between the electrostatic potential at the middle of the ribbon and at the edges, ΔV_H, is an order of magnitude higher for the structure with smaller C_C. Since the ribbon width w is the same for both structures, this leads to higher effective transverse electric field $\bar{E} \sim \frac{\Delta V_H}{w/2}$ for the case of SiO_2 structure, which, in turn, modifies the band structure of the GNR. Note that the effect of the electric field on the band structure and the DOS of graphene nanoribbons was reported before by many authors, resulting in, e.g., the energy gap modulation for semiconductor armchair ribbons[30] or opening of the energy gap for the case of zigzag ribbons.[31] This effect was also observed in bilayer structures making possible tuning of energy gap.[32]

We demonstrated above that the analytical and the numerical dependencies $C_Q = C_Q(V_Q)$ show an excellent agreement in the considered gate voltage intervals both for HfO_2 and SiO_2 structures [i.e., the utilization of Eq. (11) is fully justified]. However, the analytical and numerical dependencies $V_Q = V_Q(V_g)$ show some discrepancy, see insets to Fig. 5(b). This, in turn, leads to a discrepancy between the analytical and numerical C_Q as a function of V_g as shown in Fig. 3(c). This discrepancy is manifest itself in the difference of the gate voltage scale and not in the difference of the magnitudes of C_Q. Using Eqs. (8) and (9), the change in V_Q can be easily related co the change in V_g, $\frac{\partial V_Q}{\partial V_g} = \frac{C_{\text{tot}}}{C_Q} = (1 + \frac{C_Q}{C_C})^{-1}$. Because for a given V_Q the analytical and numerical C_Q are practically the same, the difference between the analytical and numerical dependencies $\frac{\partial V_Q}{\partial V_g}$ is primarily due to the difference of the corresponding classical capacitances C_C. We therefore conclude that the discrepancy between the analytical and numerical C_Q as a function of V_g is related to the difference in the corresponding classical capacitances.

Let us now discuss experimental determination of the quantum capacitance C_Q. In our both analytical and numerical approaches we are in position to calculate C_Q directly. In contrast, C_Q is not directly accessible in experiments. For example, for the case of carbon nanotubes it is the total capacitance C_{tot} that is measured experimentally. The quantum capacitance C_Q is then extracted from C_{tot} according to Eq. (9), $C_Q^{-1} = C_{\text{tot}}^{-1} - C_C^{-1}$, where C_C is a corresponding analytical expression for the classical capacitance of a nanotube (i.e., a classical capacitance between a metallic cylinder and an infinite plane).[11,13] Our calculations presented above demonstrate that for the graphene nanoribbons the numerical C_C differs from its classical analytical expression given by Eq. (17). Therefore, a question arises, to what extent one can rely on the above procedure for the extraction of the quantum capacitance?

In order to answer this question let us assume that our numerically calculated C_{tot} [shown in Fig. 3(b)] corresponds to the experimental data. We then assume that the classical capacitance of the GNR is given by the analytical expression (17) describing a capacitance between a metallic strip and an infinite plane. Finally, the quantum capacitance (which we will call "extracted," $C_Q^{\text{extracted}}$) is obtained by subtracting C_C from the "measured" C_{tot} according to Eq. (9). The extracted quantum capacitance is shown in Fig. 3(c). For the case of the HfO_2 structure (where $C_C \lesssim C_Q$), the behavior of $C_Q^{\text{extracted}}$ is qualitatively similar to that of the numerical C_Q, even though their values differ significantly. However, for the case of SiO_2 structure (where $C_C \ll C_Q$) the extracted quantum capacitance $C_Q^{\text{extracted}}$ does not reproduce the numerical C_Q even qualitatively with all the features related to the quantum mechanical DOS being completely lost. This is simply related to the fact that due to the series addition of the capacitances, for the case of $C_C \ll C_Q$ the total capacitance is completely dominated by the classical one, and the features in C_Q can be reproduced only when C_C becomes comparable to C_Q. It is interesting to note that the difference between the experimentally extracted quantum capacitance and its expected value was detected for the case of the carbon nanotubes and was attributed to the strong electron correlation and signatures of the Luttinger liquid behavior.[13] Our calculations indicate that the origin of such deviations can have a rather simple explanation related to the inability of a standard electrostatics to reproduce quantitatively the classical capacitance of the structure at hand.

V. CONCLUSIONS

In the present paper we develop an analytical theory for gate electrostatics and classical and quantum capacitance of GNRs. We compare the analytical theory with the exact self-consistent numerical calculations based on the tight-binding p-orbital Hamiltonian within the Hartree approximation.

We find that the analytical theory is in a good qualitative (and in some aspects quantitative) agreement with the exact calculations. There are however some important discrepancies. In order to understand the origin of these discrepancies we investigate the self-consistent electronic structure and the charge density distribution in the GNRs obtained from the exact numerical calculations. We demonstrate that the assumptions appropriate for a classical capacitor (the charge density is homogeneous and the potential of the conductor is constant) are violated for the graphene nanoribbons which leads to the difference between the analytical theory and the numerical calculations. In turn, the failure of the classical electrostatics is traced to the quantum mechanical effects leading to the significant modification of the self-consistent charge distribution in comparison to the noninteracting electron pictures. We also show that as a result of electron-electron interaction the band structure of the GNRs modifies as the applied gate voltage increases.

Our exact numerical calculations show that the density distribution and the potential profile in the GNRs are qualitatively different from those in conventional split-gate quantum wires with a smooth electrostatic confinement where the potential is rather flat and the electron density is constant throughout the wire. At the same time, the electron distribu-

tion and the potential profile in the GNR are very similar to those in the CEOQW exhibiting triangular-shaped quantum wells in the vicinity of the wire boundaries accompanied by the corresponding enhancement of the electron density close to the edges. This similarity reflects the fact that both the CEOQWs and the GNRs correspond to the case of the hard-wall confinement at the edges of the structure.

Finally, we discuss experimental determination of the quantum capacitance C_Q. We demonstrate that the extracted C_Q might significantly deviate from its actual value given by the density of states of the GNRs. This deviation is related to the inability of the standard electrostatics to reproduce quantitatively the classical capacitance of the structure at hand.

ACKNOWLEDGMENTS

A.A.S. and I.V.Z. acknowledge the support of the Swedish Research Council (VR) and the Swedish Institute (SI). J.W.K. acknowledges the support of the Polish Ministry of Science and Higher Education within the program *Support of International Mobility, 2nd edition*.

APPENDIX A: DENSITY OF STATES OF GRAPHENE NANORIBBONS

The density of states of a quantum wire (including a factor 2 for the spin degeneracy) reads,

$$\rho(E) = \left(\frac{2}{\pi}\right)\sum_n \left(\frac{dE_n(k_\parallel,k_{\perp n})}{dk_\parallel}\right)^{-1}, \tag{A1}$$

where $k_\parallel(E)$ and $k_{\perp n}$ denote the longitudinal (continuous) and the transverse (quantized) components of the wave vector, respectively. The summation in Eq. (A1) includes all transverse modes which energy $E_n \leq E$. The dispersion relation for the nanoribbon of the width N in the low-energy limit close to the Dirac point is given by Onipko,[28]

$$E^\sigma(k_\parallel) = \pm\frac{\sqrt{3}}{2}ta\sqrt{(k_\parallel - \bar{k}_\parallel^\sigma)^2 + k_{\perp n}^{\sigma 2}}, \tag{A2}$$

where $\sigma = A, Z$ corresponds to the armchair (A) and zigzag (Z) GNRs. The transverse wave vector $k_{\perp n}^A$ is given by different expressions depending on whether $\frac{2(N+1)}{3}$ is integer (metallic nanoribbon) or not (semiconducting nanoribbon),

$$k_{\perp n}^A = \begin{cases} \dfrac{\pi|n|}{N+1}\left(1 + \dfrac{\pi n}{4\sqrt{3}(N+1)}\right)a, & \text{metallic} \\ \dfrac{\pi}{N+1}\left(n - \dfrac{1}{3}\right)a, & \text{semiconducting} \end{cases}, \tag{A3}$$

$n = 0, \pm 1, \pm 2, \ldots$. For the zigzag structures, the transverse wave vector $k_{\perp n}^Z$ has a form:

$$k_{\perp n}^Z = \frac{\pi\left(n + \dfrac{1}{2}\right)}{2\sqrt{3}N}, \tag{A4}$$

$n = 0, 1, 2, \ldots$. The parameter $\bar{k}_{\perp n}^\sigma$ describes the shift of n-th dispersion branch minima respect to the Brillouin zone center,

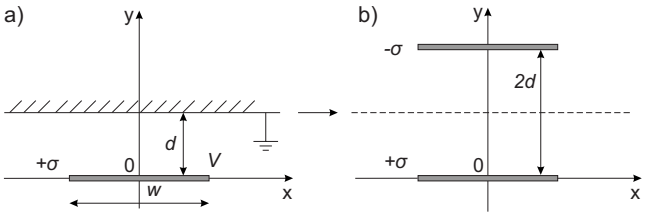

FIG. 6. (a) The capacitance formed between the metallic strip of width w located at the distance d apart from the infinite conducting plate; (b) application of the method of images to the system.

$$\bar{k}_{\perp n}^\sigma = \begin{cases} 0 & \text{for } \sigma = A \\ \dfrac{2}{3}\pi + \dfrac{\sqrt{3}}{4}k_{\perp n}^{\sigma 2} & \text{for } \sigma = Z \end{cases} \tag{A5}$$

Using Eq. (A2) in Eq. (A1), we obtain for the DOS of the armchair (zigzag) ribbon

$$\rho^\sigma(E) = \frac{4}{\pi\sqrt{3}ta}\sum_n \frac{|E|}{\sqrt{E^2 - E_n^{\sigma 2}}}\theta(|E| - |E_n|), \tag{A6}$$

where $n = 0, \pm 1, \pm 2, \ldots$ for the armchair GNRs and $n = 0, 1, 2, \ldots$ for the zigzag GNRs, and $E_n^\sigma = \pm\frac{\sqrt{3}}{2}tak_{\perp n}^\sigma$ are the subband threshold energies. The electron density at zero temperature is obtained by the integration of the DOS from the charge neutrality point $\mu_0 = 0$ to the Fermi energy, $n = \int_0^{E_F}\rho dE$,

$$n^\sigma(E_F) = \frac{4}{\pi\sqrt{3}ta}\sum_n \sqrt{E_F^2 - E_n^{\sigma 2}}\theta(|E_F| - |E_n^\sigma|). \tag{A7}$$

APPENDIX B: CAPACITANCE OF A CONDUCTING STRIP

In this Appendix we calculate the electrostatic potential and the classical capacitance between a long metallic strip of the width w and a semi-infinite conducting plate situated at the distance d from the strip as illustrated in Fig. 6(a). The potential between the strip and the plate is given by

$$V = \int_0^d E(y)dy, \tag{B1}$$

where we choose the integration path along the y axis passing through the middle of the strip ($x = 0$), and $E(y)$ is the electric field intensity along the integration path. Note that because of the symmetry of the system the electric field along the y axis has only the y component, $\mathbf{E}(x = 0, y) = E_y(y)\mathbf{y} \equiv E(y)\mathbf{y}$.

In order to calculate the electric field we use the method of images and replace the structure at hand by two oppositely charged strips as illustrated in Fig. 6(b). The electric field $E(y)$ is then given by

$$E(y) = E^{\text{strip}}(y) + E^{\text{strip}}(2d - y), \tag{B2}$$

where the second term corresponds to the mirror charges and

$$E^{\text{strip}}(y) = \frac{\sigma}{\pi\varepsilon_0\varepsilon_r}\arctan\left(\frac{w}{2y}\right) \tag{B3}$$

is the electric field intensity along the y axis passing through the middle of the conducting strip with the surface electron density σ. The last expression is obtained in a standard way by dividing the strip into infinitely narrow strips of the width $dw \to 0$ (which can be regarded as the line charges) and summing up their contributions to the electric field intensity at the point y at the y axis. Substituting Eqs. (B2) and (B3) into Eq. (B1) and performing integration, we obtain

$$V = \frac{\sigma}{\pi\varepsilon_0\varepsilon_r}\left[2d\arctan\frac{w}{4d} + \frac{w}{4}\ln\left\{1 + \left(\frac{4d}{w}\right)^2\right\}\right], \tag{B4}$$

Finally, the capacitance of the system is computed according to its definition

$$C = \frac{Q}{V} = \pi\varepsilon_0\varepsilon_r w\left[2d\arctan\frac{w}{4d} + \frac{w}{4}\ln\left\{1 + \left(\frac{4d}{w}\right)^2\right\}\right]^{-1}. \tag{B5}$$

[1] K. S. Novoselov, A. K. Geim, S. V. Morozov, D. Jiang, Y. Zhang, S. V. Dubonos, I. V. Grigorieva, and A. A. Firsov, Science **306**, 666 (2004).

[2] Y. Q. Wu, P. D. Ye, M. A. Capano, Y. Xuan, Y. Sui, M. Qi, J. A. Cooper, T. Shen, D. Pandey, G. Prakash, and R. Reifenberger, Appl. Phys. Lett. **92**, 092102 (2008).

[3] S. Luryi, Appl. Phys. Lett. **52**, 501 (1988).

[4] F. Giannazzo, S. Sonde, V. Raineri, and E. Rimini, Nano Lett. **9**, 23 (2009).

[5] Z. Chen, Y.-M. Lin, M. J. Rooks, and P. Avouris, Physica E (Amsterdam) **40**, 228 (2007).

[6] M. Y. Han, B. Özyilmaz, Y. Zhang, and P. Kim, Phys. Rev. Lett. **98**, 206805 (2007).

[7] X. Li, X. Wang, L. Zhang, S. Lee, and H. Dai, Science **319**, 1229 (2008).

[8] F. Molitor, A. Jacobsen, C. Stampfer, J. Güttinger, T. Ihn, and K. Ensslin, Phys. Rev. B **79**, 075426 (2009).

[9] X. Jia, M. Hofmann, V. Meunier, B. G. Sumpter, J. Campos-Delgado, J. M. Romo-Herrera, H. Son, Y.-P. Hsieh, A. Reina, J. Kong, M. Terrones, and M. S. Dresselhaus, Science **323**, 1701 (2009).

[10] Ç. Ö. Girit, J. C. Meyer, R. Erni, M. D. Rossell, C. Kisielowski, Li Yang, Ch.-H. Park, M. F. Crommie, M. L. Cohen, S. G. Louie, and A. Zettl, Science **323**, 1705 (2009).

[11] S. Ilani, L. A. K. Donev, M. Kinderman, and P. L. McEuen, Nat. Phys. **2**, 687 (2006).

[12] J. Liang, D. Akinwande, and H.-S. Philip Wong, J. Appl. Phys. **104**, 064515 (2008).

[13] J. Dai, J. Li, H. Zeng, and X. Cui, Appl. Phys. Lett. **94**, 093114 (2009).

[14] P. Pomorski, L. Pastewka, C. Roland, H. Guo, and J. Wang, Phys. Rev. B **69**, 115418 (2004).

[15] J. Fernández-Rossier, J. J. Palacios, and L. Brey, Phys. Rev. B **75**, 205441 (2007).

[16] J. Guo, Y. Yoon, and Y. Ouyang, Nano Lett. **7**, 1935 (2007).

[17] T. Fang, A. Konar, H. Xing, and D. Jena, Appl. Phys. Lett. **91**, 092109 (2007).

[18] K. Natori, Y. Kimura, and T. Shimizu, J. Appl. Phys. **97**, 034306 (2005).

[19] P. K. Park and S. Kang, Appl. Phys. Lett. **89**, 192905 (2006).

[20] B. Özyilmaz, P. Jarillo-Herrero, D. Efetov, and P. Kim, Appl. Phys. Lett. **91**, 192107 (2007).

[21] A. H. Castro Neto, F. Guinea, N. M. R. Peres, K. S. Novoselov, and A. K. Geim, Rev. Mod. Phys. **81**, 109 (2009).

[22] S. Dresselhaus and G. Dresselhaus, *Physical Properties of Carbon Nanotubes* (World Scientific, Singapore, 1998).

[23] S. Ihnatsenka and I. V. Zozoulenko, Phys. Rev. B **73**, 075331 (2006); I. V. Zozoulenko and S. Ihnatsenka, J. Phys.: Condens. Matter **20**, 164217 (2008).

[24] S. Ihnatsenka and I. V. Zozoulenko, Phys. Rev. B **74**, 075320 (2006).

[25] N. M. R. Peres, J. N. B. Rodrigues, T. Stauber, and J. M. B. Lopes dos Santos, J. Phys.: Condens. Matter **21**, 344202 (2009).

[26] H. Xu, T. Heinzel, M. Evaldsson, and I. V. Zozoulenko, Phys. Rev. B **77**, 245401 (2008).

[27] C. G. Broyden, Math. Comput. **19**, 577 (1965); D. Singh, H. Krakauer, and C. S. Wang, Phys. Rev. B **34**, 8391 (1986).

[28] A. Onipko, Phys. Rev. B **78**, 245412 (2008).

[29] P. G. Silvestrov and K. B. Efetov, Phys. Rev. B **77**, 155436 (2008).

[30] C. Ritter, S. S. Makler, and A. Latgé, Phys. Rev. B **77**, 195443 (2008).

[31] Y.-W. Son, M. L. Cohen, and S. G. Louie, Nature (London) **444**, 347 (2006).

[32] E. V. Castro, K. S. Novoselov, S. V. Morozov, N. M. R. Peres, J. M. B. Lopes dos Santos, J. Nilsson, F. Guinea, A. K. Geim, and A. H. Castro Neto, Phys. Rev. Lett. **99**, 216802 (2007).